



This is a repository copy of *Thermomechanical processing route to achieve ultrafine grains in low carbon microalloyed steels*.

White Rose Research Online URL for this paper:
<http://eprints.whiterose.ac.uk/104405/>

Version: Accepted Version

Article:

Gong, P., Palmiere, E.J. orcid.org/0000-0002-4048-8536 and Rainforth, W.M. orcid.org/0000-0003-3898-0318 (2016) Thermomechanical processing route to achieve ultrafine grains in low carbon microalloyed steels. *Acta Materialia*, 119. pp. 43-54. ISSN 1359-6454

<https://doi.org/10.1016/j.actamat.2016.08.010>

Reuse

This article is distributed under the terms of the Creative Commons Attribution-NonCommercial-NoDerivs (CC BY-NC-ND) licence. This licence only allows you to download this work and share it with others as long as you credit the authors, but you can't change the article in any way or use it commercially. More information and the full terms of the licence here: <https://creativecommons.org/licenses/>

Takedown

If you consider content in White Rose Research Online to be in breach of UK law, please notify us by emailing eprints@whiterose.ac.uk including the URL of the record and the reason for the withdrawal request.



eprints@whiterose.ac.uk
<https://eprints.whiterose.ac.uk/>

Thermomechanical processing route to achieve ultrafine grains in low carbon microalloyed steels

P. Gong, E.J. Palmiere, W.M. Rainforth*

Department of Materials Science and Engineering, The University of Sheffield, Sir Robert
Hadfield Building, Mappin Street, Sheffield, S1 3JD, UK

Abstract

A new thermomechanical processing route is described for a microalloyed steel, with roughing deformation below the recrystallisation-stop temperature ($T_{5\%}$), followed by a rapid reheat to 1200°C for 10s, and then finish deformation at the same temperature as the rough deformation. The new route focused on optimising the kinetics of strain-induced precipitation (SIP) and the formation of deformation-induced ferrite transformation (DITF). For comparative purposes, two experimental 0.06 wt% C steels were studied: one with 0.03 wt% Nb (Nb steel), and a second with both 0.03 wt% Nb and 0.02 wt% Ti (Nb-Ti steel). Two processing routes were studied. The first was a conventional route, which consisted of a simulated rough deformation schedule with the final roughing pass taking place at 850°C, which produced fully unrecrystallised austenite grains during deformation with no strain-induced ferrite formation. The second, new, thermomechanical processing route used the same roughing step, after which the steels were reheated at 10°C/s to a temperature of 1200°C, isothermally held for 10s allowing for precipitate dissolution, prior to air cooling to a finishing deformation temperature of 850°C. This route resulted in DIFT primarily on the prior-austenite grain boundaries. The precipitate solution during the reheat treatment increased the supersaturation of Nb and Ti in the austenite matrix on subsequent cooling, which therefore increased the undercooling due to the increased A_{e3} . The observation of

nanoscale cementite in the DIFT supports the view that it formed through a massive transformation mechanism. The volume fraction of SIP after finish deformation was influenced by the supersaturation of microalloy elements in solution during heat treatment. The new process route led to a significant refinement of the final ferrite grain size.

Keywords: Microalloyed steel; Thermomechanical controlled processing; Strain-induced precipitation; deformation-induced ferrite transformation.

*Corresponding author: m.rainforth@sheffield.ac.uk

1. Introduction

Thermomechanical controlled processing (TMCP), consisting of controlled hot rolling followed by controlled cooling, is used to maximise the benefits of the microalloy additions present in microalloyed steels [1, 2]. The improvement in mechanical properties is due to ferrite grain refinement, which maximises the surface area-to-volume ratio (S_v) of austenite grain boundaries and the deformation band density [3, 4]. However, high energy consumption and high rolling loads are a limiting factor for TMCP. Therefore, to address some of the limitations inherent with conventional TMCP, a new thermomechanical processing route has been developed to increase the finish rolling temperature in order to reduce the rolling load and improve the productivity.

Microalloyed steels have been widely utilised because of their enhanced mechanical properties over conventional steels. As is well known, each microalloy addition behaves in a different way; Ti additions enable microstructural refinement by limiting grain coarsening during reheating, while Nb facilitates a high S_v as a result of the strain-induced precipitation

of niobium carbides, nitrides or carbonitrides in the austenite. Furthermore, the Nb which remains in solution provides solute drag and through the precipitation of carbides/carbonitrides can subsequently contribute to dispersion hardening either during or after phase transformation [5-7]. Numerous studies of the precipitation kinetics focus on the fully equilibrated isothermal heat treatment in austenite with the retardation of the recrystallisation by precipitation [8] or isothermal austenite to ferrite transformation at the intercritical region [9]. However, there is limited research on the precipitation and dissolution behaviour at the non-fully equilibrated condition of steels containing one or more microalloy element, as well as their influence on the deformation structures.

The $\gamma \rightarrow \alpha$ phase transformation temperature is influenced by the deformation schedule, which therefore determines whether deformation induced ferrite (DIFT) is produced or not. Promoting DIFT has become a favoured method to obtain ultrafine ferrite grains in microalloyed low carbon steels [10-16]. Most of these investigations into DIFT have focused on the effect of chemical composition, the cooling rate and the deformation parameters (strain, strain rate). It has also been observed that a finer prior austenite grain size before deformation increases the extent of DIFT [17]. In the present study, in contrast to the observations of [17], DIFT has been promoted by a larger prior-austenite grain size, promoted by a reheating process between rough and finish deformation, with the aim to refine the final grain size in the transformed product. The mechanism of DIFT formation has been investigated through the role of precipitation, strain and the morphology of the grains as a function of deformation, as well as following isothermal holding after deformation.

2. Experimental procedures

2.1. Material

The materials used in the research consisted of two laboratory cast microalloyed steels containing Nb (designated “Nb steel”), and Nb and Ti (designated “Nb-Ti steel”), which were made by vacuum induction melting and cast into ingots having dimensions 220 mm × 65 mm × 28 mm at ArcelorMittal. The composition of the steels was analysed by Sheffield Testing Laboratories and is listed in Table 1. The ingots were soaked at 1300°C for 2 h and hot-rolled from 28 mm to 12 mm thick plates in two passes utilising a 2-high fully-instrumented 50 tonne Hille deformation mill with a finishing temperature of 1100°C followed by an ice water quench. Plane strain compression (PSC) specimens, having a geometry of 60 mm long × 30 mm wide × 10 mm high were machined from the hot rolled and as-quenched plate. PSC testing was performed using the thermomechanical compression (TMC) machine at The University of Sheffield [18]. Samples were reheated to 1100°C, held for 30s and then force-air cooled to the roughing deformation temperature of 850°C. This unusually low roughing temperature of 850°C was chosen as it was below the recrystallisation-stop temperature ($T_{5\%}$) for each steel. Deformation was undertaken in a single pass using a strain of 0.3 with a constant true strain rate of 10 s^{-1} . Immediately after roughing, the steels were rapidly reheated at a rate of 10°C/s to a temperature of 1200°C, held for 10s, followed by force-air cooling to 850°C at a rate of 10°C/s , with the finishing deformation passes being performed with different deformation parameters. The deformation and heat treatment schedule is illustrated in Fig. 1. Condition A was deformed to a strain of 0.3 at a strain rate of 10/s, and immediately quenched (designated “0s” as there was no hold at temperature). Condition B underwent the same deformation schedule as condition A, but with a 10s hold prior to quenching. Condition C underwent the same thermomechanical schedule as condition B, but then received an additional strain of 0.3 at a strain rate of 10/s followed by an immediate water quench. This

material had therefore received a total finish deformation strain of 0.6. Finally, condition D received the same thermomechanical schedule as condition C, but with a final 10s hold prior to water quenching.

Table 1
Chemical composition of the experimental steels (wt%)

| | C | Si | Mn | Cr | Ni | Nb | Ti | N | P |
|-------------|-------|------|------|------|------|-------------|-----------------|--------|-------|
| Nb steel | 0.067 | 0.11 | 0.77 | 0.01 | 0.02 | 0.03 | <0.01 | 0.0058 | 0.016 |
| Nb-Ti steel | 0.065 | 0.11 | 0.77 | 0.01 | 0.02 | 0.03 | 0.02 | 0.0062 | 0.016 |

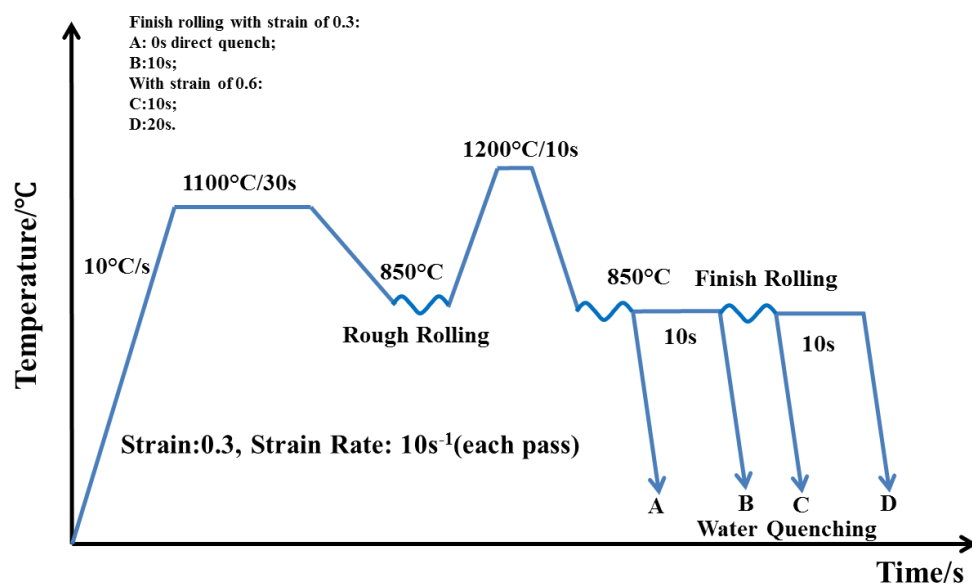


Fig. 1 Schematic of the thermomechanical cycles used and nomenclature used for each condition.

2.2. Grain size and microstructure

Longitudinal specimens were prepared for metallographic examination using standard techniques. The polished specimens were etched in a solution of saturated picric acid at 60°C to reveal the prior-austenite grain boundaries. The average austenite grain size was measured using the linear intercept method (ASTM E-112) by optical microscopy (OM). Scanning electron microscopy (SEM) was used to observe the microstructures of ferrite and martensite, which was etched using a 2% nital solution for approximately 5-10s. Electron backscatter diffraction (EBSD) was used to measure the final sub-grain size after finish deformation from

the Nb-Ti steel. Samples for EBSD were prepared by the same method as the SEM samples. The acceleration voltage of 20kV and an emission current of around 80 μ A were chosen with the step size of 300nm. The minimum misorientation angle that defines a grain boundary was set to 2°. Misorientation angles between 2° and 15° were regarded as low-angle grain boundaries, while those larger than 15° were designated high-angle grain boundaries.

2.3. Precipitate analysis

Transmission electron microscopy (TEM) was carried out to identify the strain-induced precipitation. Carbon extraction replicas were prepared in the standard manner using a light 2% nital etch. Subsequent thin foils were electropolished using an electrolyte solution of 5% perchloric acid, 35% butoxyethanol and 60% methanol. Extraction replica samples and thin foil samples were examined in FEI Tecnai T20 and JEOL 2010F TEM. The particle diameter distribution of precipitates was measured for each sample, with around 200 particles counted in each case, with quantitative image analysis being performed using Image J software. Additionally, chemical analysis of the precipitates was conducted using an Oxford instruments energy dispersive X-ray spectroscopy (EDX) detector (Oxford Instruments, Oxford, UK) and electron energy loss spectroscopy (EELS) analysis, using a Gatan GIF. The measurement of the sample thickness was also carried out using EELS. This was estimated from the low energy region of the spectrum, given by Eq. (1) [19,20]:

$$t = \lambda \ln(I_t/I_0) \quad (1)$$

where t represents the thickness of material; λ is the mean free path of specimen; I_t is the total number of electrons in the EEL spectrum and I_0 is the number of electrons in the zero loss peak.

3. Results

3.1 Microstructures

Optical micrographs, Fig. 2, revealed typical prior-austenite grain morphologies, all taken from the normal direction (ND). The average prior-austenite grain size was $31.3 \pm 0.6 \mu\text{m}$ in the Nb steel and $29.1 \pm 0.5 \mu\text{m}$ in the Nb-Ti steel after reheating at 1100°C for 30s before roughing deformation (see deformation schedule in Fig. 1). Following the roughing deformation at 850°C , the average prior-austenite grain size was subsequently refined to $18.7 \pm 1.6 \mu\text{m}$ for the Nb steel and $16.9 \pm 0.7 \mu\text{m}$ for the Nb-Ti steel, Fig. 2 (a) and (b), respectively. After roughing deformation followed by reheating to 1200°C for 10 s the average grain size increased to $86.4 \pm 5.5 \mu\text{m}$ for the Nb steel (Fig. 2 (c)), and $50 \pm 3.5 \mu\text{m}$ for the Nb-Ti steel (Fig. 2 (d)). Fig. 2 (e) and (f), show typical prior-austenite grain morphologies after finish deformation at 850°C , schedule A, for the Nb and Nb-Ti steels. Ferrite was located mainly on the prior-austenite grain boundaries.

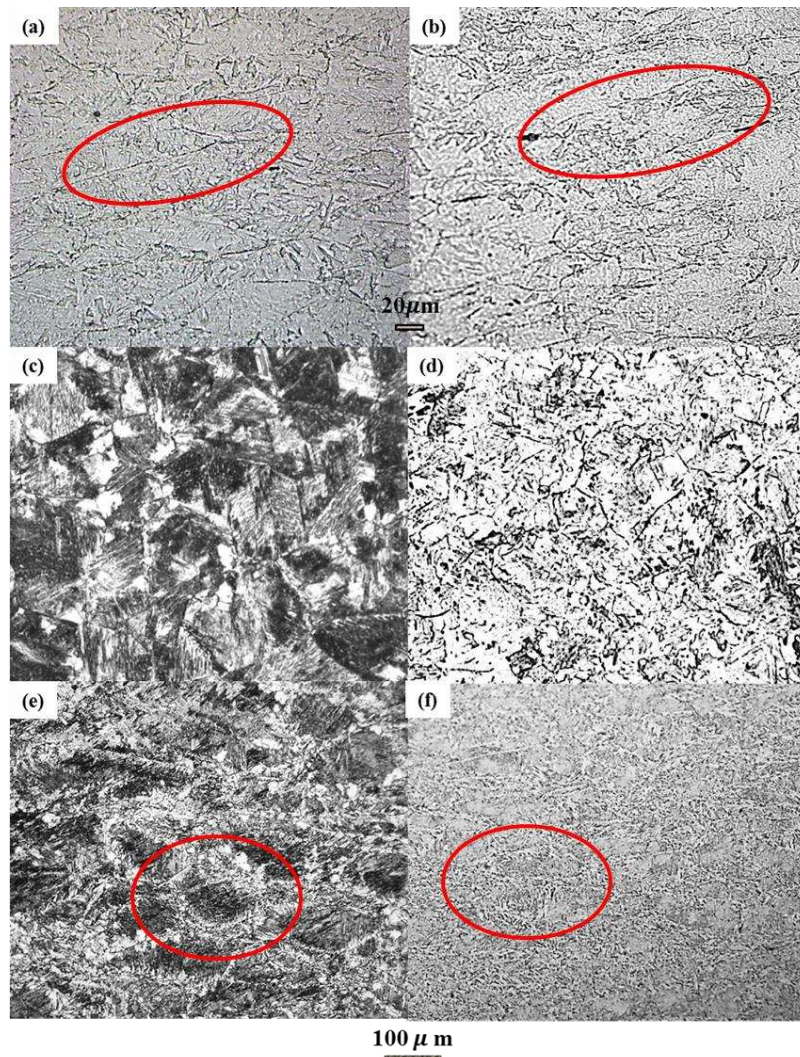


Fig. 2 Optical microstructures of prior-austenite grains in the Nb and Nb-Ti steels: (a), (c) and (d) for the Nb steel; (b), (d) and (e) for the Nb-Ti steel; (a) and (b) after roughing deformation at 850°C; (c) and (d) after roughing deformation at 850°C followed by heat treatment at 1200°C for 10s; (e) and (f) finish deformation with schedule A (Fig. 1) (the red circles in the Fig. 2 (a) and (b) show the elongated prior austenite grain boundaries and in the Fig. 2 (e) and (f) show the bowed grain boundaries).

Fig. 3 gives the average prior-austenite grain size, measured as a function of isothermal holding time during finish deformation and steel composition. The average prior-austenite grain size in the Nb steel was larger than that in the Nb-Ti steel for the same holding time. For both Nb and Nb-Ti steels, the average grain size was refined with increasing strain, and the isothermal 10s holding after deformation at 850°C.

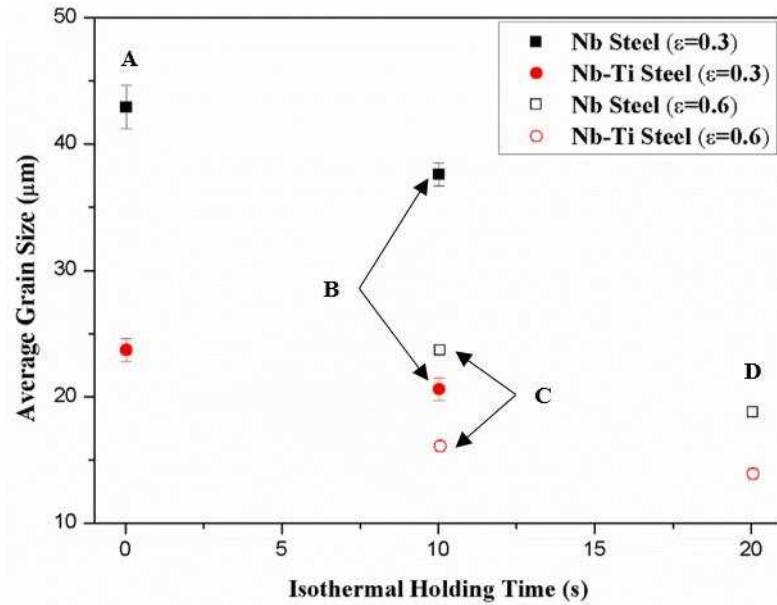


Fig. 3 Average prior-austenite grain size in the Nb and Nb-Ti steels with isothermal holding time.

In order to investigate the effect of the prior-austenite grain size and morphology on transformation, samples were water quenched after the reheat at 1100°C for 30s prior to rough deformation (Fig. 4 (a) and (b)), after rough deformation (Fig. 4 (c) and (d)) and after a hold at 1200°C for 10s after rough deformation and prior to finish deformation (Fig. 4 (e) and (f)). This shows that the recrystallisation texture after 10s at 1200°C was closely related to the deformation texture after rough deformation at 850°C for both steels, but different from the recrystallisation textures after 30s at 1100°C prior to rough deformation.

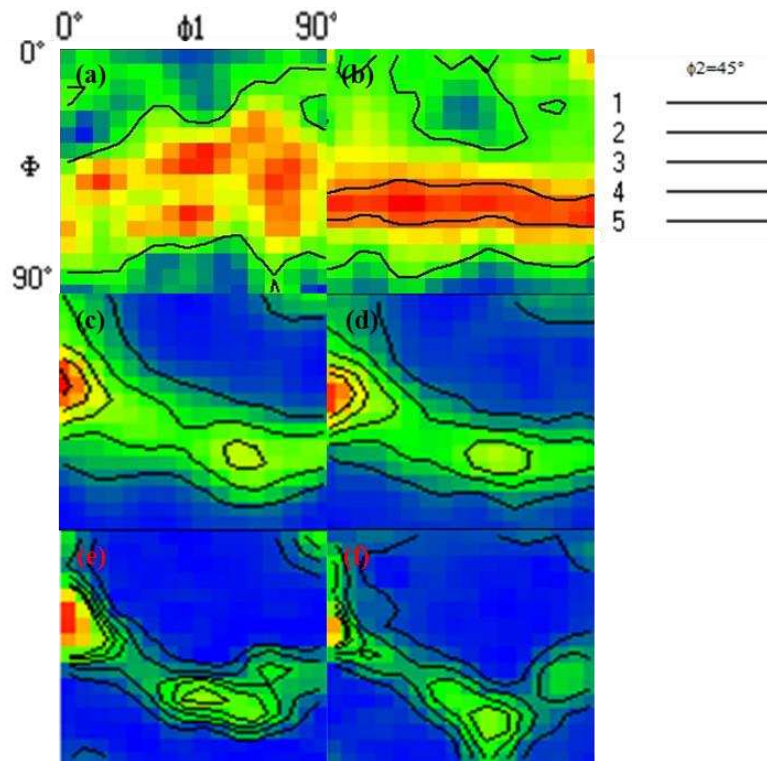


Fig. 4 $\phi_2=45^\circ$ sections of ODFs from rough deformation and reheating Nb and Nb-Ti steels; (a) reheating at 1100°C for 30s for Nb steel; (b) reheating at 1100°C for 30s for Nb-Ti steel (c) rough deformation at 850°C for Nb steel; (d) rough deformation at 850°C for Nb-Ti steel; (e) reheating at 1200°C for 10s for Nb steel; (f) reheating at 1200°C for 10s for Nb-Ti steel.

Fig. 5 shows EBSD maps where the boundaries $>15^\circ$ disorientation have been labelled. The prior-austenite grain size was much larger at 1200°C for 10s after rough deformation and prior to finish deformation (Fig. 5 (b) and (d)), when compared with 1100°C for 30s prior to rough deformation (Fig. 5 (a) and (c)). In addition, while the Nb steel exhibited a broadly equiaxed structure after 30s at 1100°C , the Nb-Ti steel had a partly bainitic structure. Following the reheat at 1200°C for 10s, both steels exhibited boundaries that were extensively serrated (Fig. 5 (b) and (d)), marked by black arrows, with the Nb-Ti steel generally showing a finer structure than the Nb steel.

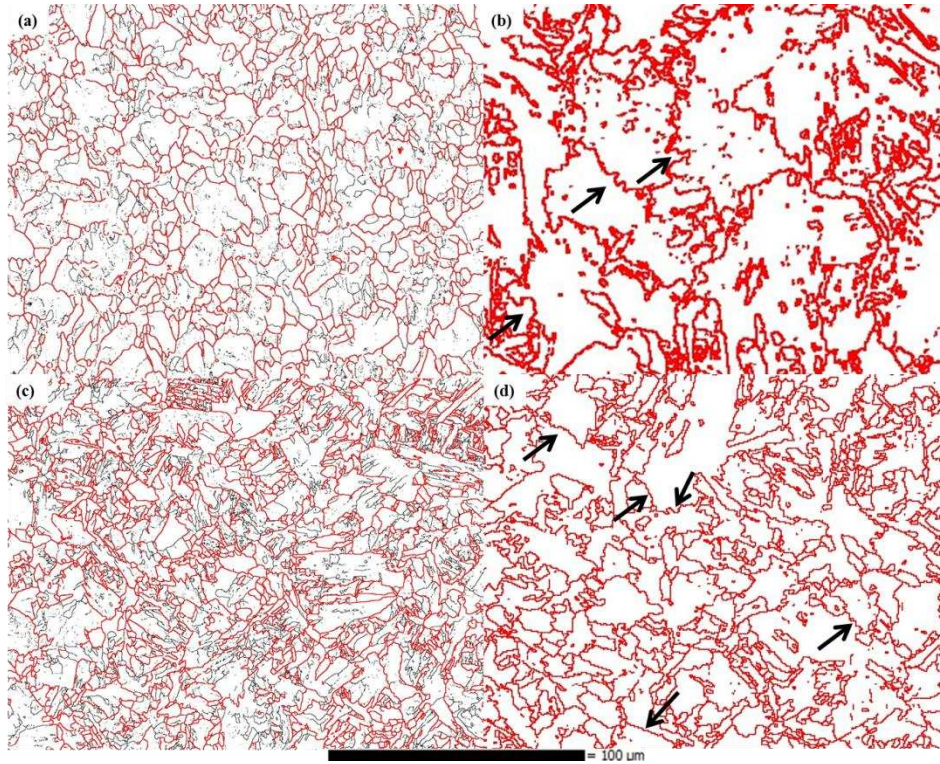


Fig. 5 EBSD analysis of the Nb and Nb-Ti steels specimen using the grain boundary map with HAGBs ($\theta \geq 15^\circ$) as red line: (a) heat treatment at 1100°C for 30 s for Nb steel; (b) heat treatment at 1200°C for 10 s for Nb steel; (c) heat treatment at 1100°C for 30 s for Nb-Ti steel; (d) heat treatment at 1200°C for 10 s for Nb-Ti steel.

3.2 Strain-induced Precipitation

The average diameter of the strain-induced precipitates (SIP) was 12.0 ± 0.7 nm in the Nb steel and 14.0 ± 0.5 nm in the Nb-Ti steel, and the volume fraction of SIP with the size less than 20 nm was measured from carbon extraction replicas as $(4.0 \pm 0.3) \times 10^{-5} \mu\text{m}^{-3}$ and $(5.4 \pm 0.36) \times 10^{-5} \mu\text{m}^{-3}$ for the respective Nb and Nb-Ti steels after roughing deformation at 850°C. After reheating to 1200°C for 10s, the Nb in solution was measured in the both Nb and Nb-Ti steels as 0.021 ± 0.001 wt% and 0.012 ± 0.0012 wt% respectively [21]. The results show that the Nb steel exhibited a higher supersaturation of Nb compared to that in the Nb-Ti steel.

Following cooling, and after finish deformation at 850°C, the volume fraction and the average diameter of SIP in the Nb and Nb-Ti steels was determined from TEM carbon replicas, Fig. 6. SIP as a function of the isothermal holding time in the Nb-Ti steel followed a similar trend to that in the Nb steel. It is clear from Figure 6 (e) that the volume fraction of SIP increased with increasing strain. It also increased with the 10s isothermal hold after deformation at 850°C when compared with water quenched samples at the same strain for both steels. The volume fraction of precipitates in the Nb steel was slightly less than in the Nb-Ti steel at the start, but after deforming to a strain to 0.6, the precipitate volume fraction was higher in the Nb steel compared to the Nb-Ti steel. With increasing strain or adding a 10s hold at the deformation temperature, the average diameter of the precipitates decreased gradually. This is a result of fresh precipitation occurring either as a result of deformation or the isothermal hold, which increased the volume fraction but reduced average precipitate diameter. The mean diameter of precipitates in the Nb steel was smaller than in the Nb-Ti steel (Fig. 6 (f)). Additionally, when comparing rough deformation and finish deformation for the same deformation parameters (i.e. one pass deformation with a strain of 0.3), the average precipitate size was refined and the volume fraction increased by finish deformation. This was due to the higher microalloy supersaturation after reheating to 1200°C, and higher undercooling between the heat treatment and finish deformation temperature. Again, this was the result of fresh precipitation reducing the average precipitate size.

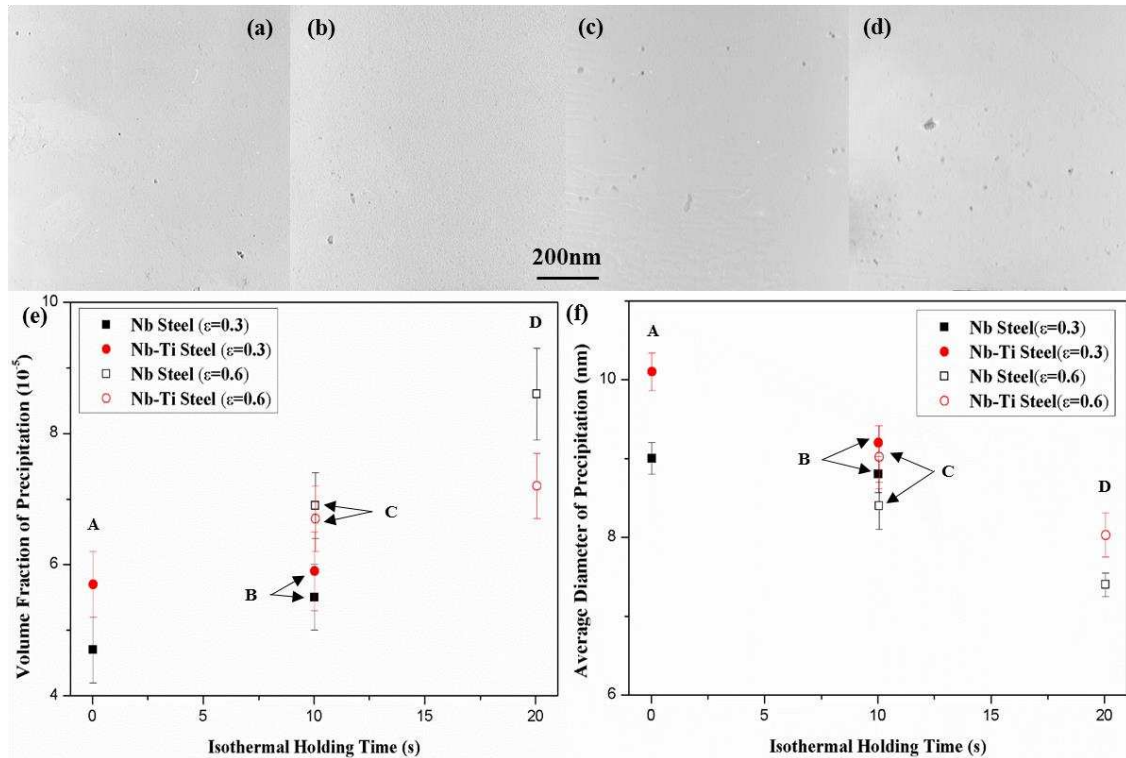


Fig. 6 TEM observation of precipitation in the Nb steel from carbon replica specimens after finish deformation with the isothermal holding time of (a) $\epsilon=0.3$, 0s (schedule A), (b) $\epsilon=0.3$, 10s (schedule B), (c) $\epsilon=0.6$, 10s (schedule C), (d) $\epsilon=0.3$, 10s + 10s hold (schedule D). (e) The volume fraction of precipitation as a function of different deformation parameters in the Nb and Nb-Ti steels. (f) The average precipitate size in the Nb and Nb-Ti steels with different rolled parameters.

Fig. 7 gives high resolution lattice images and EDX spectra from the precipitates, which was taken from typical specimens after processing with the schedule of C for both Nb and Nb-Ti steels. The crystal structure was identified using the inverse fast Fourier transformation (IFFT). Fig. 7 (a) shows an HRTEM image of a spherical shaped particle from the Nb steel. The corresponding inverse fast Fourier transform (Fig. 7 (b)) indicates a $[110]_{MC}$ zone axis with the measured d spacing about 0.25 nm, which is close to published values for the $d_{(111)}$ spacing of NbC of 0.258 nm. The chemical composition of the particle was measured by EDX with the Nb L line (Fig. 7 (c)). The structure and EDX results suggest that, as expected, the precipitates were NbC in the Nb steel. The HRTEM image of a cuboid precipitate is presented in Fig. 7 (d) from the Nb-Ti steel specimen with the same deformation schedule of Nb steel. The structure and the composition of the SIP was analysed by IFFT image (Fig. 7

(e)) and EDX spectrum (Fig. 7 (f)). The IFFT image suggests that this particle has a d spacing about 0.21 nm along the zone axis of $[100]_{MC}$. The EDX spectrum shows the Ti M and Nb L lines. The $d_{(002)}$ spacing of (Nb,Ti)C is about 0.216 nm with the lattice parameter of 0.432 nm [22]. The particle in Fig. 7 (d) is identified as (Nb,Ti)C in the Nb-Ti steel.

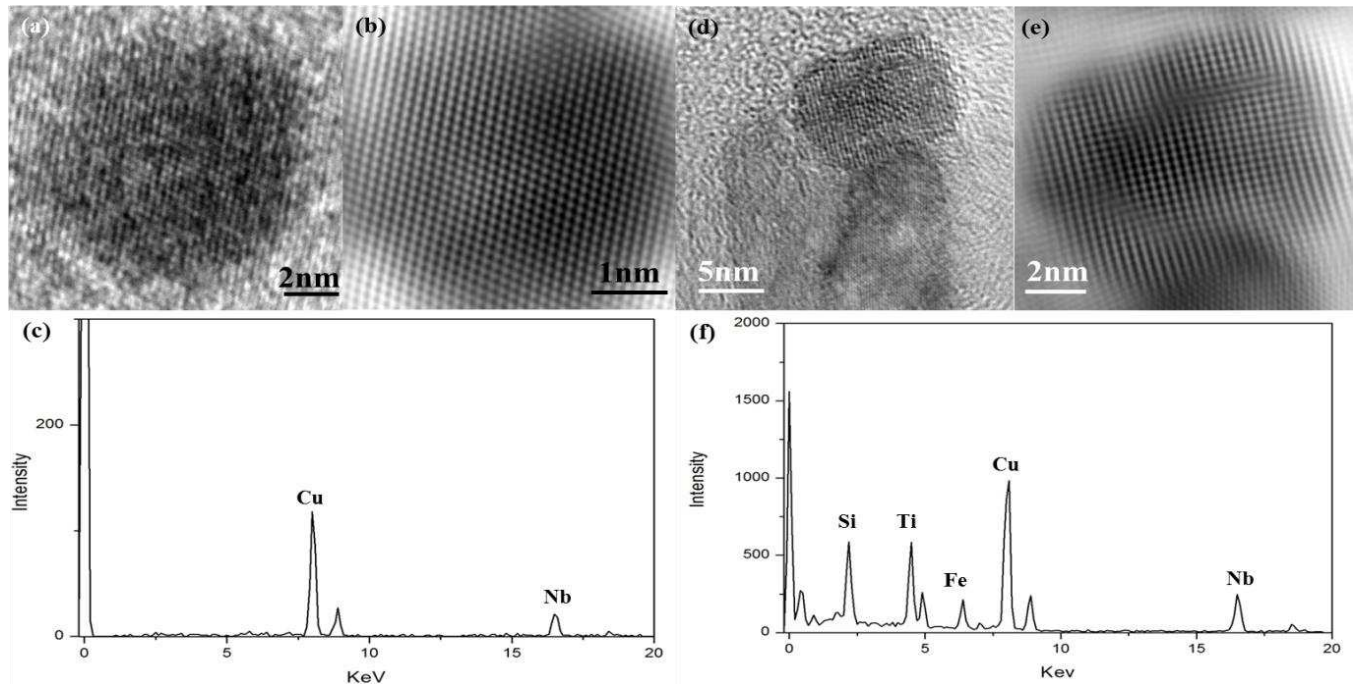


Fig. 7 The morphology and the composition of SIP with the schedule of C: (a) HRTEM image, (b) IFFT lattice image and (c) EDX spectrum of the nanometer scale carbide in the Nb steel; (d) HRTEM image, (e) IFFT lattice image and (f) EDX spectrum of the nanometer scale carbide in the Nb-Ti steel.

3.3 Deformation induced transformation ferrite (DIFT)

Fig. 8 shows typical deformation induced ferrite (black arrow) and martensite structures from the Nb and Nb-Ti steels after finish deformation with the schedule of A, where the DIFT was primarily located at the prior-austenite grain boundaries. The morphology of the DIFT and martensite after finish deformation with holding time of 10s (schedule B), 10s (schedule C) and 20s (schedule D) were similar with that at 0s. The volume fraction of DIFT as a function of deformation parameters was calculated from SEM images and is shown in Fig. 9. It can be

seen that the volume fraction of DIFT in the Nb-Ti steel was larger than that in the Nb steel for each process condition. The volume fraction of DIFT increased with increasing strain for both Nb and Nb-Ti steels. It also increased with the 10s isothermal hold after deformation for a given strain. After a one pass deformation and holding for 10s at 850°C, there was a much higher volume fraction of DIFT than after the finish deformation without subsequent hold (schedule A). The volume fraction of DIFT increased with increasing strain to 0.6, but with a decreasing rate as the strain increased (schedule C and D).

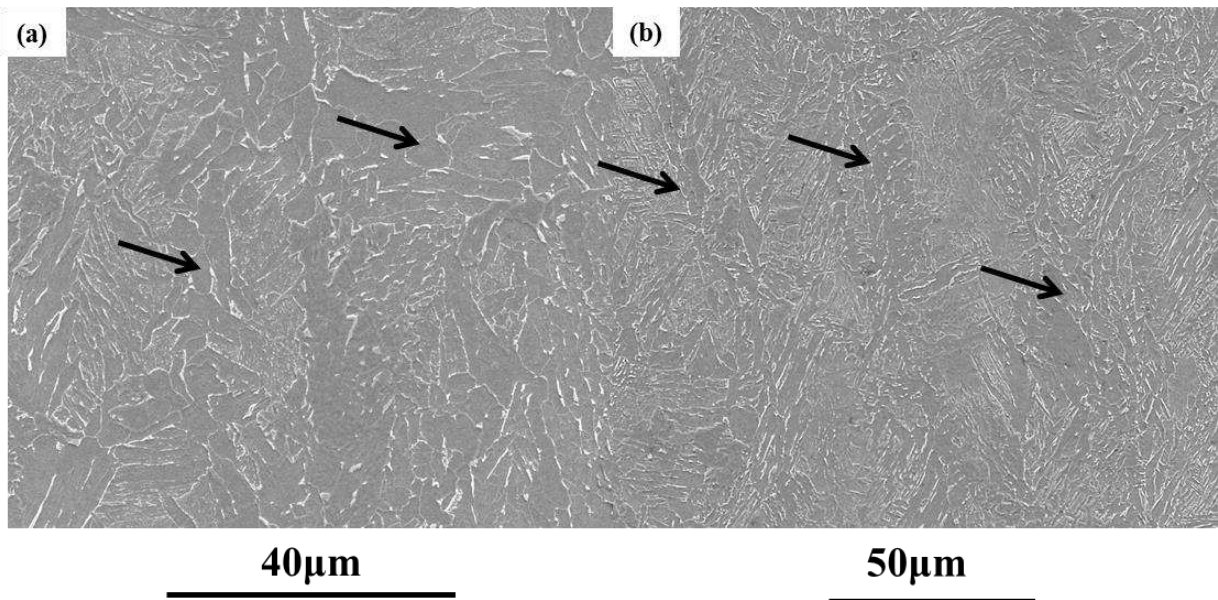


Fig. 8 SEM observation of DIFT for both Nb and Nb-Ti steels after finish deformation with the schedule of A:
(a) Nb steel; (b) Nb-Ti steel.

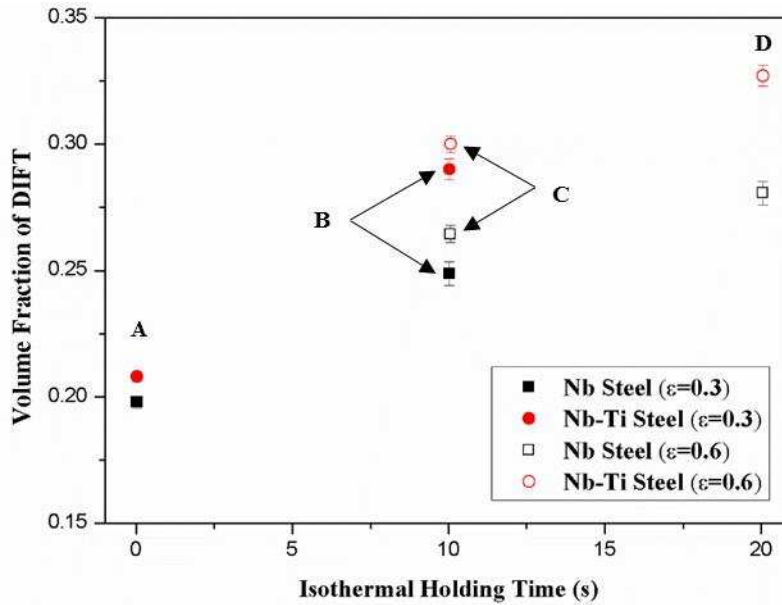


Fig.9 The variation of volume fraction of DIFT as a function of isothermal holding time in the Nb and Nb-Ti steels.

3.4 Nano-scale cementite in DIFT

Nanoscale cementite was observed in the DIFT. Typical morphologies of cementite after finish deformation using the D schedule are shown in Fig. 10. Bright field images, Fig. 10 (a) and (b), show nanoscale cementite particles in the ferrite matrix (red arrow) for both Nb and Nb-Ti steels with few of them located on sub-grain boundaries. The diffraction pattern in Fig. 10 (c), which corresponds to the image of Fig. 10 (b), shows the orientation relationship of the body-centred cubic ferrite matrix and the orthorhombic cementite. Fig. 10 (d) shows a lattice image of a nanometer-sized cementite particle taken from the same sample shown in Fig. 10 (a). The inverse fast Fourier transformation (IFFT) (Fig. 10 (e)) with corresponding diffractogram (Fig.10 (f)) was used to analyse the lattice spacing and orientation shown in Fig. 10 (d). This shows that the TEM observation was along the $[2\bar{4}5]_{\text{Fe}_3\text{C}}$ zone axis with the intersection of $(\bar{2}10)$ and (132) as 120° . The ferrite d spacing was identified as $d_{(01\bar{1})}$, $\sim 0.202\text{nm}$. In Fig. 10 (f), the diffraction spot marked by the red arrow was a result of Moiré fringing with the spacing of parallel Moiré fringes about 0.53 nm. The Moiré fringes were

produced due to the two interaction vectors from the cementite ($d_{(132)}$) and ferrite ($d_{(01\bar{1})}$) with the intersection angle β of 8.5° . Then the spacing of Moiré fringes can be calculated using the Eq. (2) [23]:

$$L = \frac{d_{ferrite} \times d_{Fe_3C}}{\left((d_{ferrite} - d_{Fe_3C})^2 + d_{ferrite} \times d_{Fe_3C} \times \beta^2 \right)^{1/2}} \quad (2)$$

where L is the spacing of Moiré fringe with the distance of 0.53 nm, and $d_{ferrite(01\bar{1})}$ is the spacing of (01 $\bar{1}$) about 0.202 nm. Thus, the d spacing of cementite was calculated using Eq. (2) to be 0.159 nm, which is close to the $d_{(132)}$ spacing of Fe₃C as 0.153 nm. This therefore confirms that the particle was Fe₃C imaged along the zone axis of $[\bar{2}45]$.

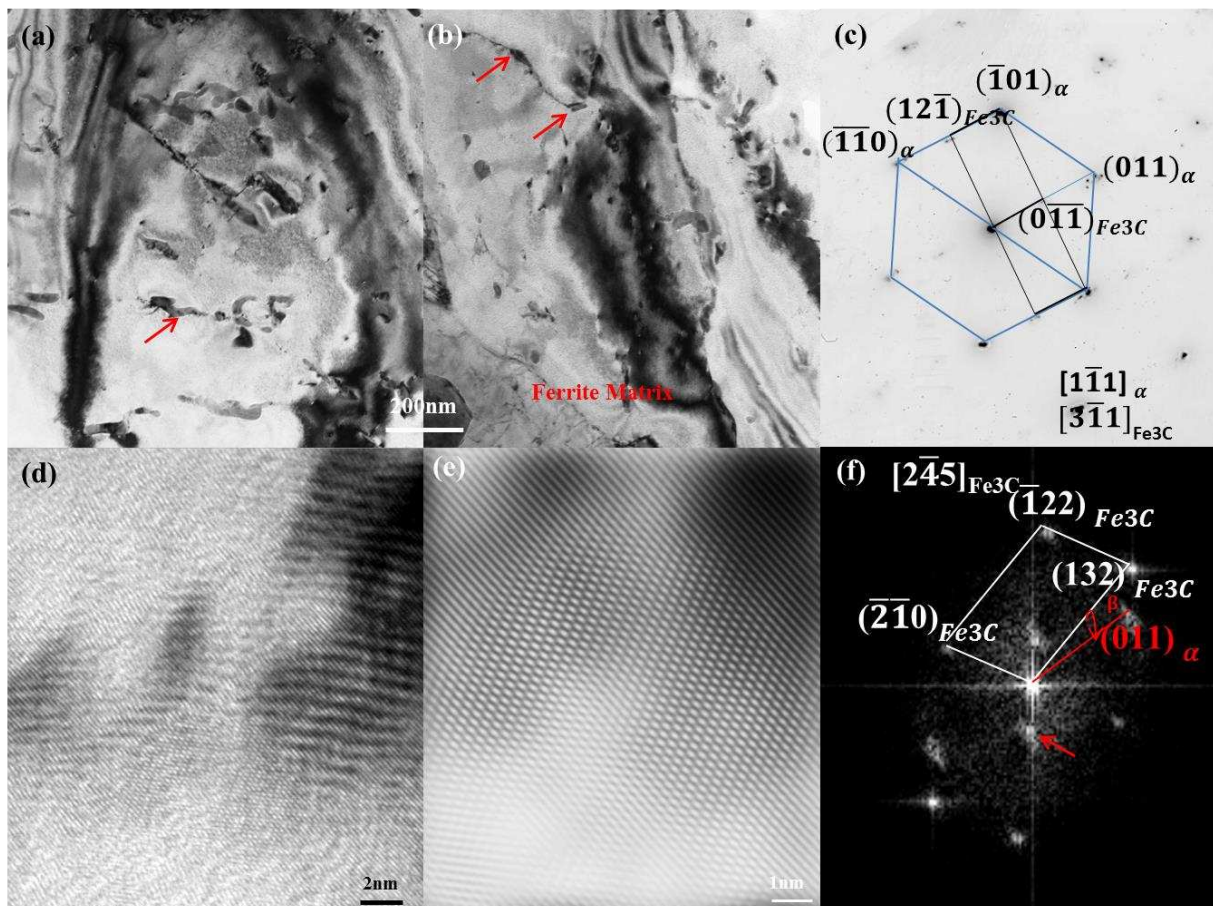


Fig. 10 The nanometer-sized Fe₃C with the deformation schedule of D: (a) Bright-field TEM micrograph of nanoscale cementite in the Nb steel and (b) Bright-field TEM micrograph of nanoscale cementite in the Nb-Ti

steel; (c) corresponding electron diffraction pattern from (a); (d) HRTEM image of one nanoscale cementite; (e) IFFT lattice image from (d); (f) the corresponding fast Fourier transformed diffractogram.

3.5 The application of DIFT to reduce the final grain size

The difference between the new thermomechanical process and the conventional methods for producing DIFT [14,24,25] was the introduction of an additional heat treatment process between roughing and finish deformation. To further test the effectiveness of this new TMCP on DIFT, and therefore on the refinement of the final grain size, an additional test program schedule was undertaken, as shown in Fig. 11. The Nb-Ti steel specimen was firstly rough rolled at 850°C, and then the temperature was rapidly increased to 1200°C and held for 10s. Following this, the temperature was reduced to 850°C and deformed with three passes, and then, finally, rapidly air cooled to 500°C with the cooling rate of 20°C/s, then at 2°C/s to room temperature. The cooling schedule was used to simulate the coiling process. The final average ferrite grain size from the Nb-Ti steel using this new TMCP route was measured at $1.40 \pm 0.05 \mu\text{m}$ by EBSD shown in Fig. 12 (a). Fig. 12 (b) shows a typical misorientation profile across a few ferrite grains along the line shown in Fig. 12 (c). As expected, a high misorientation angle was observed across adjacent grain boundaries. Therefore, this new TMCP route produced an ultra-fine ferrite grain size with high angle grain boundaries attributed to DIFT of austenite to ferrite with low deformation strains.

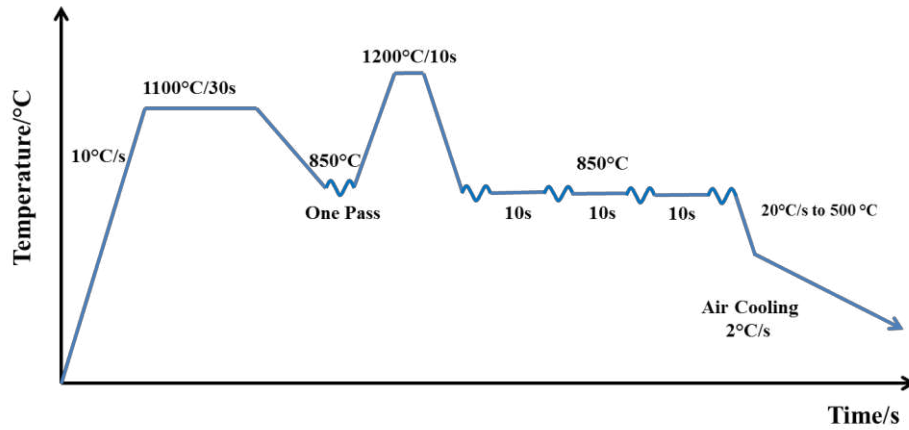


Fig. 11 Laboratory deformation schedule for the production of ultrafine grains on the Nb-Ti steel.

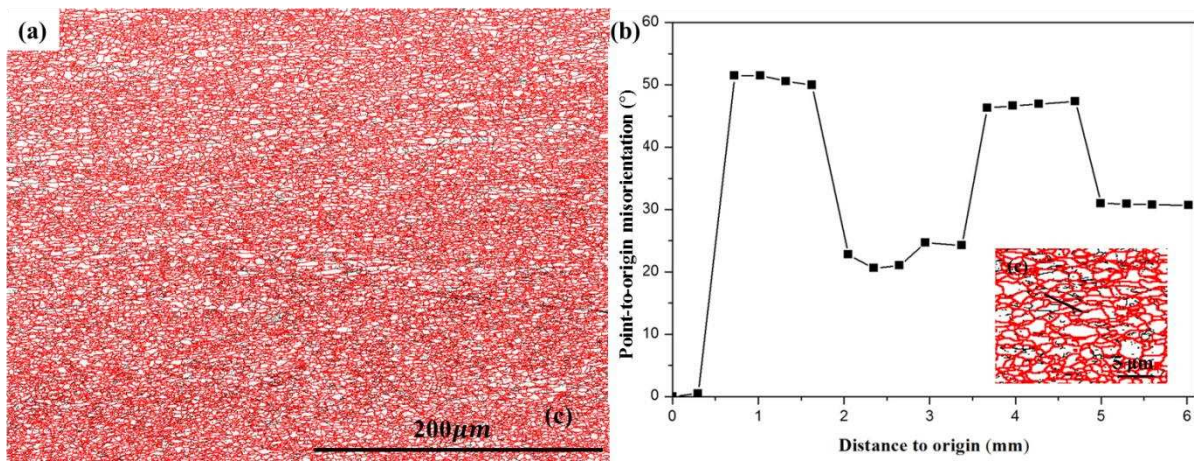


Fig. 12 (a) Ultra-fine grain boundary with IPF maps obtained by EBSD from Nb-Ti steel after deformation by the process shown in Fig. 11; (b) Point-to-origin misorientation profiles from (a); (c) grain boundaries with higher magnification from (a) (labelled).

4. Discussion

4.1 The effect of deformation and precipitation on the prior-austenite grain size after TMCP

Fig. 2 shows the elongated prior-austenite grain structures after finish deformation below the recrystallisation-stop temperature ($T_{5\%}$). The prior-austenite grain size in the ND was measured as a function of the different isothermal holding time, Fig. 3. As expected, the grain

size was refined with an increase in strain which will have led to an increase in the volume fraction of SIP, and hence a greater Zener pinning force. There are several models that predict this behaviour. First, the theory of grain refinement as a function of strain was proposed by Sellars [26], where the kinetic behaviour of the prior-austenite grain size as a function of deformation can be calculated by:

$$d(t)=0.9 \times d_0^{0.67} \times \varepsilon^{-0.67} \quad (3)$$

where d_0 is the reheated grain size and ε is the true strain of the finish deformation deformation. The predicted grain diameter in the Nb steel is 39.5 μm (schedule A) and 24.9 μm (schedule C), shown in Fig. 13 (a). In the Nb-Ti steel, the predictions are 27.7 μm for (schedule A) and 17.4 μm for (schedule C) (Fig. 13 (b)). The predicted data using Eq. (3) for both Nb and Nb-Ti steels fit well with the experimental data of the prior-austenite grain size.

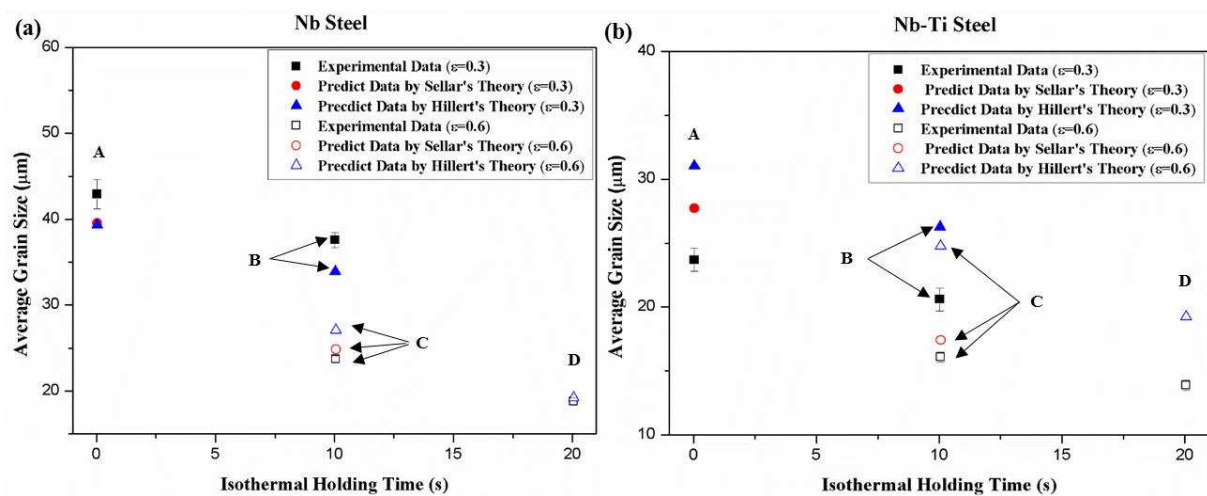


Fig. 13 simulated average grain size with isothermal holding time, compared with experimental data by Eqs. (3) and (4): (a) in the Nb steel; (b) in the Nb-Ti steel.

The change in the prior-austenite grain size during deformation is also related to the extent of SIP. In the classic work of Zener (as reported by Smith [27]), it was shown that the grain growth can be retarded when the free energy of a migrating boundary is equal to that of the

restriction of the boundary by precipitates. As such, it is predicted that the mean grain diameter, \bar{D} , is correlated to the volume fraction of SIP. However, this theory still has weaknesses; for example, it does not consider the relative positions of the particles with respect to the boundary and neglects abnormal grain growth. Therefore, Hellman and Hillert [28] modified the original model of Zener for the pinning effect of second-phase particles on grain boundaries:

$$\frac{D_{max}}{D_p} = 4\left(\frac{D_{max}}{\bar{D}} - 1\right) / 3f_v \quad (4)$$

where D_{max} is the largest limiting grain diameter; D_p is the mean second phase particle diameter; the \bar{D} is the mean grain diameter; f_v is the volume fraction of particles. Hellman and Hillert also indicated that the ratio of $\frac{D_{max}}{\bar{D}}$ should be in the range of 1-2 to account for the limiting grain growth. Considering the experimental data of the maximum and mean grain size after the deformation schedule A, the ratio of $\frac{D_{max}}{\bar{D}}$ was assumed to be 1.3 for the Nb steel and 1.2 for the Nb-Ti steel. Then, using the data of volume fraction (f_v) and the average diameter (D_p) of precipitates shown in Fig. 6, the simulated mean grain size was calculated by Eq. (4) and is presented in Fig. 13 (a) for the Nb steel and Fig. 13 (b) for the Nb-Ti steel. The predicated grain size for the Nb steel using the Hellman and Hillert's theory fits well with the experimental data after finish deformation with different isothermal holding time. However, for the Nb-Ti steel the data predicted by Hellman and Hillert's theory are slightly larger than the experimental data. This is because of the significantly higher DIFT in the Nb-Ti steel than in the Nb steel (Fig. 9), which will have significantly reduced the average grain size, which of course is not taken into account in Hellman and Hillert's theory.

4.2 The influencing factors on the volume fraction of SIP

The rapid reheating to 1200°C for 10s after rough deformation at 850°C would have gradually dissolved the SIP that formed during rough deformation and the Nb dissolution rate was faster in the Nb steel than in the Nb-Ti steel [21]. The volume fraction and average diameter of SIP after finish deformation was analysed by TEM and is shown in Figs. 6 and 7. The average diameter of the SIP was much smaller and the volume fraction of the SIP higher after finish deformation (schedule A) than that after rough deformation for the same deformation parameters for both Nb and Nb-Ti steels. As expected, the increased supersaturation led to a higher driving force for precipitation in both Nb and Nb-Ti steels [29,30]. Furthermore, the volume fraction of SIP and its average diameter was also directly influenced by the amount of deformation. By increasing the strain to 0.6 during finish deformation, the volume fraction of SIP increased and its average size reduced due to the deformation stored energy which increased the driving force for precipitation [31,32].

For the samples that were subject to a 10 s hold at 850°C after either the first or second pass of finishing deformation, the volume fraction of SIP (Fig. 6) was also higher than in those samples that were immediately water quenched. This is in agreement with many publications for precipitation kinetics [6,33,34], which shows that the 10s hold at 850°C can provide sufficient incubated time for precipitation. As expected, for a strain of 0.6 during finish deformation, the effect of the 10s hold at 850°C on the volume fraction of SIP was higher than that at the lower strain of 0.3, especially for the Nb steel. In addition, the average diameter of the SIP was also refined. Therefore, the 10s hold time combined with the deformation during finish deformation were the main factors leading to the refined size and increased volume fraction of precipitation.

During rough deformation, the volume fraction of SIP for the Nb steel ($(4.0 \pm 0.3) \times 10^{-5} \mu\text{m}^{-3}$) was lower than that for Nb-Ti steel ($(5.4 \pm 0.36) \times 10^{-5} \mu\text{m}^{-3}$), because of the lower total microalloy content in the Nb steel. After reheating to 1200°C for 10s, the Nb in solution in the Nb steel was higher than that in the Nb-Ti steel. The difference in volume fraction of SIP between the Nb and Nb-Ti steels after finish deformation to a strain of 0.3 followed by immediate water quenching was smaller than that during roughing deformation. Furthermore, the volume fraction of SIP for Nb steel was higher than that in the Nb-Ti steel during finish deformation for an increased strain of 0.6 in finish deformation (Fig. 6 (e)). The result indicates that, with adequate deformation strain, the effect of supersaturation on the precipitation behaviour was significant, as expected.

4.3 Mechanisms leading to DIFT

DIFT was only observed under specific processing conditions. It was not observed in either steel after conventional thermomechanical processing (i.e. roughing deformation followed by finish deformation). However, the introduction of a 1200°C hold after roughing deformation resulted in the formation of DIFT for otherwise identical TMP conditions as the conventional thermomechanical process conditions. The extent of DIFT formed on the larger prior austenite grains was greater in the Nb-Ti steel than in the Nb steel. The extent of DIFT also increased with the introduction of an additional 10s hold during finish deformation. These observations are not easy to explain, but the following sections consider each of the potential factors.

4.3.1 Effect of process conditions on the γ/α transformation temperature

The upper equilibrium temperature between ferrite and austenite, A_{e3} , and the ferrite start temperature, A_{r3} , can be calculated using different models considering the weight percentage of alloying elements. In this study, the equilibrium phase transformation temperature of A_{e3} was calculated by Eq. (5) for low carbon steels [35]. The Blas et al. [36] model was considered for the simulation of the $\gamma \rightarrow \alpha$ start transformation temperature (A_{r3}), which was derived for a low carbon content between 0.024-0.068 %wt and is expressed as Eq. (6):

$$A_{e3} = 871 - 254.4\sqrt{\%C} - 14.2\%Ni + 51.7\%Si \quad (5)$$

$$A_{r3} = 903 - 328(\%C) - 102(\%Mn) + 116(\%Nb) - 0.909v \quad (6)$$

where v is cooling rate with $^{\circ}\text{C}/\text{s}$. In the present study, the carbon content was 0.065 %wt for the Nb steel and 0.067 %wt for the Nb-Ti steel (Table 1 lists the compositions used), which satisfied the range of applicability for Eqs. (5) and (6). The A_{e3} for both Nb and Nb-Ti steels was 870°C derived from Eq. (5). The A_{r3} temperature was calculated from Eq. (6) as 796°C for both steels, which is lower than the deformation temperature of 850°C .

It is well known that the equilibrium phase transformation free energy (ΔG_v) related with the chemical driving force, the volume strain energy and interface energy can be increased by the deformation [37], which expressed by:

$$\Delta G_v = V(\Delta G_{chem} + \Delta G_D - \Delta G_S) - A\sigma_{\alpha\gamma} \quad (7)$$

where ΔG_{chem} is the chemical driving force; ΔG_D is the deformation stored energy; ΔG_S is the volume strain energy; and $\sigma_{\alpha\gamma}$ is the interface energy. From Eq. (7), this accumulated energy from deformation can raise the equilibrium $\gamma \rightarrow \alpha$ transformation temperature, which is the upper limit transformation temperature for DIFT, A_{ed3} shown in Fig. 14. Therefore, the higher

transformation temperature of A_{ed3} increases the undercooling (ΔT), which accelerates the phase transformation rate.

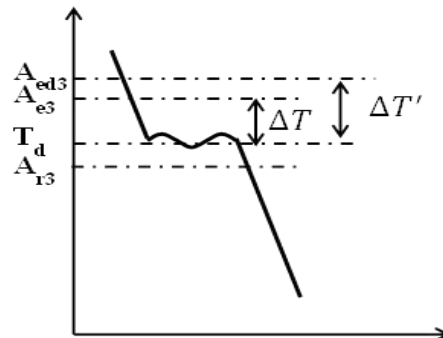


Fig. 14 Schematic of the undercooling that influenced by the deformation with the increasing of equilibrium phase transformation temperature.

The microstructures after roughing deformation at 850°C followed by water quenching are shown in Fig. 2 (a) and (b), in which no ferrite was observed at the prior-austenite grain boundaries. This shows that the roughing deformation occurred in the single austenite phase region. Thus, the increased undercooling arising from the deformation did not provide sufficient driving force for the phase transformation during deformation. In contrast, after finish deformation with the same parameters used in the roughing deformation, but with a 1200°C hold in between, a small amount of ferrite was formed on and within the prior-austenite grain boundaries (Figs. 2 (e), (f) and Fig. 8). Given that the steels experienced the same roughing deformation and finish deformation parameters, the only difference between them was the heat treatment at 1200°C and therefore this was responsible for the observation of DIFT after finish deformation.

Eqs. (5) and (6) do not predict the difference in DIFT being observed by the introduction of the 1200°C heat treatment, and do not predict that DIFT is more extensive in the Nb-Ti steel than in the Nb steel. Eqs. (5) and (6) do not take account of the difference between the Nb and Ti being tied up with carbon in precipitates or being in solution in the austenite. Clearly,

without the 1200°C hold, the majority of the Nb and Ti will have been present in the form of precipitates, while following the hold at 1200°C, the Nb and Ti were predominantly in solution in the austenite. This suggests that by taking the Nb and Ti into solution, the A_{ed3} temperature was increased and the extent of the increase in A_{ed3} was greater for the Nb-Ti steel compared to the Nb steel. The clear difference in transformation behaviour between the two steels can be seen in Fig. 5, where the Nb steel produced an equiaxed ferritic structure upon quenching, whereas the Nb-Ti steel exhibited a bainitic structure.

4.3.2 Size and morphology of prior austenite grain size

As shown in Fig. 2, the DIFT formed on the larger prior austenite grain boundaries after finish deformation (Fig. 2 (e) and (f)), but was not observed on the prior-austenite grain boundaries after the initial roughing deformation (Fig. 2 (a) and (b)). Normally, long-range diffusion theory is used to explain DIFT. Austenite grain coarsening would suppress the ferrite transformation and limit the number of nucleation sites. This is because the ferrite mainly nucleates at deformed prior-austenite grain boundaries at lower strains [37], such that more DIFT would be expected to form for smaller grain sizes because of the higher grain boundary area [37]. However, the results in this study demonstrated that the larger prior-austenite grain size led to greater DIFT, suggesting that long range diffusion was not a factor during this phase transformation [38], [39]. Beynon et al. [40] and Hurley et al. [41] also reported that a coarse austenite grain size appeared to be more favourable for DIFT under the condition of single pass deformation, because the formation of pro-eutectoid ferrite was prevented resulting in a large undercooling. However, they did not give further explanation for their observations.

In this study, the observation that a coarser prior-austenite grain size led to more DIFT suggests that the mechanism of DIFT is controlled by short-range diffusion across α/γ interfaces, consistent with a massive transformation to form the deformation induced ferrite. In addition, nanoscale cementite was observed in the deformation induced ferrite, Fig. 10. This was believed to arise because the fast strain rate and associated rapid formation of DIFT limited the carbon diffusion to austenite matrix during phase transformation, resulting in supersaturated ferrite. According to the Kaufman-Radcliffe-Cohen (KRC) thermodynamic model [42], the supersaturated DIFT will have formed ferrite and spherical cementite (Fe_3C) during subsequent cooling, as shown in Fig. 15. Therefore, the formation of nanoscale Fe_3C within the DIFT also suggests a massive transformation for the DIFT.

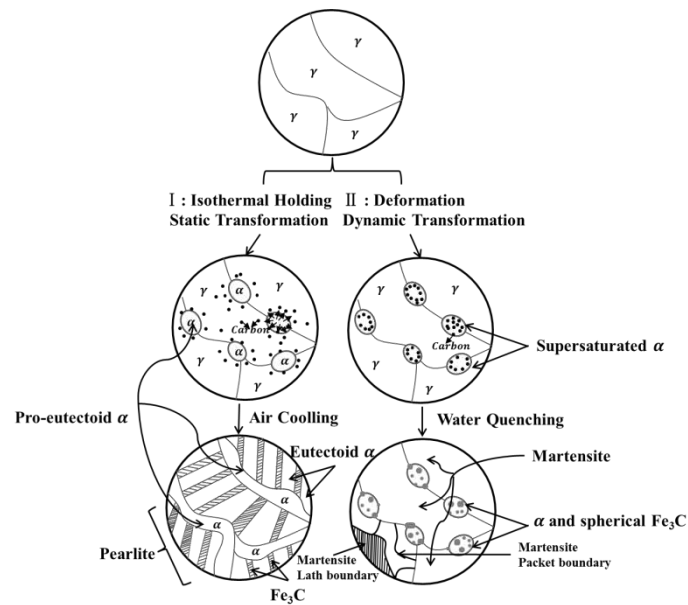


Fig. 15 Schematic illustration of the transformation from austenite: I Static transformation; II Dynamic transformation.

Fig. 4 gave ODFs taken from EBSD maps from the roughing rolled and reheated Nb and Nb-Ti steels and showed that the recrystallisation texture (after 10s at 1200°C) was closely related to the deformation texture after roughing deformation at 850°C for both steels, but

different from the recrystallization textures after heat treatment at 1100°C for 30s [43]. This suggests that the strain-induced boundary migration (SIBM) mechanism was dominant during recrystallisation, as reported by several researchers [43–45]. The SIBM would have probably left irregular grain boundaries, with serrations that could act as preferential sites for DIFT. This is also consistent with the serrations observed in the EBSD maps in Fig. 5 showing the grain boundary structure after the 1200°C reheat followed by an immediate quench. Sun et al. [46] reported that DIFT preferentially forms on the serrations and bulging prior-austenite grain boundaries due to the local higher energy. Therefore, the coarser prior-austenite grain structure, with boundaries that exhibited serrations and bulging, would have promoted more DIFT than a finer, equiaxed, grain size, which further supports the view that DIFT is controlled by short-range diffusion across α/γ interfaces.

5. Conclusions

A new thermomechanical controlled process route has been developed to obtain deformation induced ferrite transformation, which has been shown to be a very effective method to refine the final grain size combined with reducing the deformation force and improvement the productivity. The study of prior-austenite grain size, the precipitation behaviour, and their effects on the formation of DIFT have been investigated, with the following conclusions:

- 1) As expected, the prior-austenite grain size decreased in the normal direction with increased strain for Nb and Nb-Ti steels. When compared with the water quenched specimens, the grain size also decreased after isothermal holding for 10 s at the deformation temperature under the same deformation strain, due to the increasing volume fraction of DIFT.
- 2) Spherically shaped strain-induced precipitates (SIP) in the Nb steel were identified as NbC, while the cuboid shaped precipitates in the Nb-Ti steel were (Nb,Ti)C. The volume

fraction of SIP increased with the increasing strain. The isothermal hold of 10s after deformation at 850°C produced more precipitation due to the incubation time available for precipitation. In addition, the reheat to 1200°C increased the supersaturation of microalloy elements in the matrix leading to a higher volume fraction and smaller diameter of SIP after finish deformation compared to roughing deformation with the same deformation parameters.

3) Sellars' theory, which considers the grain refinement as a function of strain, fitted well with the experimental data. Hellman and Hillert's modified Zener pinning model provided a good prediction of the grain size with the experimental data for volume fraction and diameter of SIP for the Nb steel. However, the match was less good for the Nb-Ti steel because of the error introduced by the formation of DIFT at the deformation temperature in this steel.

4) DIFT occurred on and within the elongated coarser prior-austenite grains during finish deformation as a result of the introduction of the reheat at 1200°C. The observation of the serrations and bulging prior-austenite grain boundaries, and nanoscale cementite formed in ferrite matrix after finish deformation supported the view that DIFT occurred through a massive transformation.

5) The volume fraction of DIFT increased with the increasing applied strain and isothermal hold after deformation. This new TMCP followed by control cooling produced a refined final grain size of $1.4 \pm 0.05 \mu\text{m}$.

Acknowledgements

The authors would like to thank both ArcelorMittal Maizières and Companhia Brasileira de Metalurgia e Mineração (CBMM) for the financial support of this research programme. The EBSD analysis supported by B.P. Wynne of The University of Sheffield is thankfully appreciated.

References

- [1] A. Ghosh, S. Das, S. Chatterjee, B. Mishra, P. Ramachandra Rao, Influence of thermo-mechanical processing and different post-cooling techniques on structure and properties of an ultra low carbon Cu bearing HSLA forging, *Mater. Sci. Eng. A* 348 (1-2) (2003) 299-308.
- [2] M.C. Zhao, K. Yang, Y.Y. Shan, The effects of thermo-mechanical control process on microstructures and mechanical properties of a commercial pipeline steel, *Mater. Sci. Eng. A* 335 (1-2) (2002) 14-20.
- [3] A. Ghosh, B. Mishra, S. Das, S. Chatterjee, An ultra low carbon Cu bearing steel: influence of thermomechanical processing and aging heat treatment on structure and properties, *Mater. Sci. Eng. A* 374 (1-2) (2004) 43-55.
- [4] M. Gomez, P. Valles, S.F. Medina, Evolution of microstructure and precipitation state during thermomechanical processing of a X80 microalloyed steel, *Mater. Sci. Eng. A* 528 (13-14) (2011) 4761-4773.
- [5] S.G. Hong, H. Jun, K.B. Kang, C.G. Park, Evolution of precipitates in the Nb-Ti-V microalloyed HSLA steels during reheating, *Scr. Mater.* 48 (8) (2003) 1201-1206.
- [6] S.G. Hong, K.B. Kang, C.G. Park, Strain-induced precipitation of NbC in Nb and Nb-Ti microalloyed HSLA steels, *Scr. Mater.* 46 (2) (2002) 163-168.
- [7] A.M. Elwazri, P. Wanjara, S. Yue, Effect of prior-austenite grain size and transformation temperature on nodule size of microalloyed hypereutectoid steels, *Metall. Mater. Trans. A* 36A (2005) 2297-2305.
- [8] B. Dutta, C.M. Sellars, Effect of composition and process variables on Nb (C, N) precipitation in niobium microalloyed austenite, *Mater. Sci. Technol.* 3 (1987) 197-206.
- [9] T. Sakuma, R.W.K. Honeycombe, Microstructures of isothermally transformed Fe-Nb-C alloys, *Met. Sci.* 18 (9) (1984) 449-454.
- [10] F. Equihua, A. Salinas, E. Nava, Effect of aluminum content on austenite-ferrite transformation temperature in low carbon (Si-Al) hot rolled GNO electrical steels, *Rev. Metal.* 46 (1) (2010) 78-85.
- [11] J. Chen, F. Li, Z.Y. Liu, S. Tang, G.D. Wang, Influence of deformation temperature on γ - α phase transformation in Nb-Ti microalloyed steel during continuous cooling, *ISIJ Int.* 53 (6) (2013) 1070-1075.
- [12] A. Imandoust, A. Zarei-Hanzaki, H.R. Abedi, Low-temperature strain-induced ferrite transformation in twinning-induced plasticity steel, *Scr. Mater.* 67 (12) (2012) 995-998.

- [13] B. Eghbali, A. Abdollah-zadeh, Strain-induced transformation in a low carbon microalloyed steel during hot compression testing, *Scr. Mater.* 54 (6) (2006) 1205-1209.
- [14] A. Ohmori, S. Torizuka, K. Nagai, N. Koseki, Y. Kogo, Effect of deformation temperature and strain rate on evolution of ultrafine grained structure through single-pass large-strain warm deformation in a low carbon steel, *Mater. Trans.* 45 (7) (2004) 2224-2231.
- [15] R. Song, D. Ponge, D. Raabe, J.G. Speer, D.K. Matlock, Overview of processing, microstructure and mechanical properties of ultrafine grained bcc steels, *Mater. Sci. Eng. A* 441 (1-2) (2006) 1-17.
- [16] P. Hodgson, M. Hickson, R. Gibbs, The production and mechanical properties of ultrafine ferrite, *Mater. Sci. Forum* 284-286 (1998) 63-72.
- [17] M.S. Loveday, G.J. Mahon, B. Roebuck, Measurement of flow stress in hot plane strain compression tests, *Mater high T.* 23 (2) (2006) 85-118.
- [18] D.C. Joy, D.M. Maher, The quantitation of electron energy-loss spectra, *J. Microsc.* 124 (1) (1981) 37-48.
- [19] R.D. Leapman, Detecting single atoms of calcium and iron in biological structures by electron energy-loss spectrum-imaging, *J. Microsc.* 210 (1) (2003) 5-15.
- [20] P. Gong, E.J. Palmiere, W.M. Rainforth, Dissolution and precipitation behaviour in steels microalloyed with niobium during thermomechanical processing, *Acta Mater.* 97 (2015) 392-403.
- [21] K. Ono, J. Moriyama, The phase relationships in the Nb-Ti-C system, *J. Less Common. Met.* 79 (2) (1981) 255-260.
- [22] D.B. Williams, C.B. Carter, *Transmission Electron Microscopy: A Textbook for Materials Science*, second ed., Springer US, 2009.
- [23] M. Bechtold, Y. Adachi, D. Ponge, D. Raabe, Deformation and fracture mechanisms in fine- and ultrafine-grained ferrite/martensite dual-phase steels and the effect of aging, *Acta Mater.* 59 (2) (2011) 658-670.
- [24] Z.Q. Sun, W.Y. Yang, J.J. Qi, A.M. Hu, Deformation enhanced transformation and dynamic recrystallization of ferrite in a low carbon steel during multipass hot deformation, *Mater. Sci. Eng. A* 334 (1-2) (2002) 201-206.
- [25] C.M. Sellars, The kinetics of softening processes during hot working of austenite, *Czech. J. Phys. B* 35 (3) (1985) 239-248.
- [26] C. Smith, Statistical studies of structure II Measurement of spatial grain size, *Trans. Amer. Inst. Min. Engrs.* 175 (1949) 15-50.

- [27] P. Hellman, M. Hillert, Effect of second-phase particles on grain growth, *Scand. J. Metall.* 4 (5) (1975) 211-219.
- [28] E.J. Palmiere, C.I. Garcia, A.J. DeArdo, Compositional and microstructural changes which attend reheating and grain coarsening in steels containing niobium, *Metall. Mater. Trans. A* 25 (1994) 277-286.
- [29] N.H. Van Dijk, S.E. Offerman, W.G. Bouwman, M.Th. Rekveldt, High temperature SANS experiments on Nb (C, N) and MnS precipitates in HSLA steel, *Mater. Trans. A* 33A (2002) 1883-1891.
- [30] T.E. Quested, A.L. Greer, Athermal heterogeneous nucleation of solidification, *Acta Mater.* 53 (9) (2005) 2683-2692.
- [31] J.W. Cahn, Transformation kinetics during continuous cooling, *Acta Metall.* 4 (6) (1956) 572-575.
- [32] S.F. Medina, The influence of niobium on the static recrystallization of hot deformed austenite and on strain induced precipitation kinetics, *Scr. Metall. Mater.* 32 (1) (1995) 43-48.
- [33] B. Dutta, E.J. Palmiere, C.M. Sellars, Modelling the kinetics of strain induced precipitation in Nb microalloyed steels, *Acta Mater.* 49 (5) (2001) 785-794.
- [34] J. Barralis, G. Maeder, *Métallurgie*, first ed., Communications actives, Paris, 1982.
- [35] A.A Gorni, *Steel forming and heat treating handbook*, Sao Vacente, Brazil, <http://www.gorni.eng.br/>, 2004.
- [36] H. Dong, X. Sun, Deformation induced ferrite transformation in low carbon steels, *Curr. Opin. Solid State Mater. Sci.* 9 (6) (2005) 269-276.
- [37] C. Capdevila, F.G. Caballero, C. Andrés, Austenite grain size effects on isothermal allotriomorphic ferrite formation in 0.37 C-1.45 Mn-0.11 V microalloyed steel, *Mater. Trans.* 44 (6) (2003) 1087-1095.
- [38] T. Massalski, Massive transformations revisited, *Metall. Mater. Trans. A* 33 (2002) 2277-2283.
- [39] H. Aaronson, Mechanisms of the massive transformation, *Metall. Mater. Trans. A* 33 (2002) 2285-2297.
- [40] J.H. Beynon, P. Gloss, P.D. Hodgson, The Production of Ultrafine Equiaxed Ferrite in A Low Carbon Steels Microalloyed Steel by Thermomechanical Treatment, *Mater. Forum* 16 (1) (1992) 37-42.
- [41] P.J. Hurley, P.D. Hodgson, Formation of ultra-fine ferrite in hot rolled strip: potential mechanisms for grain refinement, *Mater. Sci. Eng. A* 302 (2) (2001) 206-214.

- [42] H.I. Aaronson, V.F. Zackay, Decomposition of austenite by diffusional processes, Interscience, New York, 1962.
- [43] K. Kashihara, Y. Takeuchi, T. Shibayanagi, Characteristics of Strain-Induced Boundary Migration as Evaluated by the Crystal Rotation Axis Method in (001) [100] and (112) [111] Aluminum Bicrystal Deformed by Plane-Strain Compression, Mater. Trans. 51 (4) (2010) 607-613.
- [44] M.C. Theyssier, J.H. Driver, Recrystallization nucleation mechanism along boundaries in hot deformed Al bicrystals, Mater. Sci. Eng. A 272 (1) (1999) 73-82.
- [45] S.P. Bellier, R.D. Doherty, The structure of deformed aluminium and its recrystallization-investigations with transmission Kossel diffraction, Acta Metall. 25 (5) (1977) 521-538.
- [46] L. Sun, K. Muszka, B.P. Wynne, E.J. Palmiere, Effect of strain path on dynamic strain-induced transformation in a microalloyed steel, Acta Mater. 66 (2014) 132-149.